



Cationic surfactant-assisted hydrothermal synthesis of few-layer molybdenum disulfide/graphene composites: Microstructure and electrochemical lithium storage

Lin Ma^{a,b}, Guochuang Huang^a, Weixiang Chen^{a,*}, Zhen Wang^a, Jianbo Ye^a, Haiyang Li^c, Dongyun Chen^d, Jim Yang Lee^d

^a Department of Chemistry, Zhejiang University, Hangzhou 310027, PR China

^b Chemistry Science and Technology School, Institute of Physical Chemistry, Zhanjiang Normal University, Zhanjiang 524048, PR China

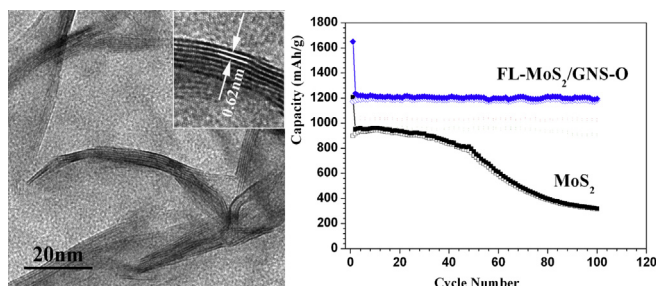
^c Department of Physics, Zhejiang University, Hangzhou 310027, PR China

^d Department of Chemical and Biomolecular Engineering, National University of Singapore, 10 Kent Ridge Crescent, 119260, Singapore

HIGHLIGHTS

- FL-MoS₂/GNS composites are prepared by a facile cationic surfactant–hydrothermal route.
- Cationic surfactants show some ability to control layer number of FL-MoS₂ in the composites.
- FL-MoS₂/GNS exhibits outstanding electrochemical properties as a reversible lithium storage host.

GRAPHICAL ABSTRACT



ARTICLE INFO

Article history:

Received 19 January 2014

Received in revised form

2 April 2014

Accepted 21 April 2014

Available online 29 April 2014

Keywords:

Few-layer molybdenum disulfide

Graphene

Composites

Cationic surfactants

Electrochemical lithium storage

ABSTRACT

Few-layer molybdenum disulfide/graphene (FL-MoS₂/GNS) composites are fabricated by a facile hydrothermal route and a post-annealing with the assistance of various cationic surfactants (dodecyltrimethylammonium bromide, DTAB; octyltrimethylammonium bromide, OTAB; and tetrabutylammonium bromide, TBAB), which have different alkyl-chain lengths and stereo configurations. The effects of these cationic surfactants on the microstructures and electrochemical performances of the FL-MoS₂/GNS for lithium storage are investigated. It is demonstrated the cationic surfactants show some ability to control the microstructure (layer number) of FL-MoS₂ in composites. The electrochemical performances of FL-MoS₂/GNS composites for lithium storage are greatly improved compared to the bare MoS₂. Especially, FL-MoS₂/GNS with ~6 MoS₂ layers prepared with the assistance of OTAB exhibits very high reversible capacity of ~1200 mAh g⁻¹ with excellent cycle stability and enhanced rate capability. Electrochemical impedance spectrum also confirms that the FL-MoS₂/GNS composite electrodes exhibit much lower electron-transfer resistance than the MoS₂. The remarkable electrochemical performances of FL-MoS₂/GNS composites can be attributed to the synergistic interaction between FL-MoS₂ and graphene and their quasi-3D architectures, which promote lithium diffusion, electron transfer and electrolyte access.

© 2014 Elsevier B.V. All rights reserved.

* Corresponding author. Tel.: +86 571 87952477; fax: +86 571 87951895.

E-mail addresses: weixiangchen@zju.edu.cn, tj88317@163.com (W. Chen).

1. Introduction

With the advent of plug-in hybrid electric vehicles and a new greater political awareness toward the importance of energy storage, the advanced energy storage and conversion technology have become an increasingly pivotal part of the modern era [1]. As the most advanced rechargeable batteries, lithium-ion batteries (LIBs) have attracted the great attention due to their high energy/power densities, long life and environment-friendly characteristics [2,3]. The capability of LIBs largely depends on the electrode materials, especially anodes. Graphite anodes have been ubiquitous in current designs but are limited by its low theoretical capacity of 372 mAh g⁻¹. Thus, it is of great significance to design and create the novel electrode materials with higher capacity, excellent cycle and rate capability for next-generation high-performance LIBs [4].

Two-dimensional (2D) nanomaterials have long been regarded as attractive materials owing to their unique properties and promising applications in energy storage and conversion, particularly for LIBs due to their shortened paths and more channels for lithium ion fast-diffusion and insertion [5,6]. Among these 2D crystals, graphene nanosheet (GNS) is an unequivocal champion and exhibits superior conductivity, high charge mobility, crystal and electronic quality [7,8]. GNS have been used as an appealing platform for preparing a variety of composites and hybrids with exceptional properties and mass potential applications [9,10]. Apart from graphene, other 2D crystal nanosheets, especially 2D transition metal dichalcogenide (TMD, such as MoS₂ and WS₂) sheets with single-layer (SL) or few-layer (FL), have recently attracted considerable attention for their unexpectedly exotic behaviors compared with the bulk counterparts [6,11]. As a typical TMD, MoS₂ crystals have a sandwich interlayer structure formed by stacking of the (S–Mo–S) layers in *c*-direction, which are loosely bound to each other by van der Waals [12]. This layered structure is favorable to exfoliation of layers into SL- or FL-MoS₂ nanosheets. Currently, the exfoliation of the bulk MoS₂ into SL- or FL-nanosheets can be achieved by mechanical cleavage [13–15] and liquid exfoliation based on N-butyllithium [16]. However, the efficiency of the former is very low and the latter consumes a large amount of organic solvent and is sensitive to environmental conditions [16,17]. A few new approaches toward the SL- or FL-MoS₂ nanosheets can be now available, such as the modified liquid exfoliation under sonication [18–20], electrochemical lithiation-assisted exfoliation [21,22], laser/plasma thinning [23] and other solution-phase approaches (e.g. hydrothermal or solvothermal synthesis [24,25], oleylamine-assisted wet-chemical approach [26]).

On another hand, nanostructured MoS₂, especially the SL- or FL-MoS₂ nanosheets, have gradually emerged as a promising electrode material for LIBs owing to their more channels and shortened paths for the fast diffusion and insertion of lithium storage [11,27,28]. Even if the SL- or FL-MoS₂ nanosheets exhibit much higher specific capacity than graphite anodes, they suffer a lot from the poor cycling stability caused by particle pulverization and restacking of nanosheets during repeated lithiation/delithiation process, and a low rate-capability originating from the intrinsic low electronic conductivity of MoS₂ [29,30]. To circumvent the above drawbacks, a feasible strategy is to combine MoS₂ nanosheets with highly conductive and flexible matrix such as carbon nanotube and graphene as a buffer layer and a current micro-collector [31–36]. GNS appears particularly promising to improve the rate capability and cycle performance of MoS₂ nanosheets owing to their superior electrical conductivity, high charge mobility, large surface area and inherent flexibility [7,34]. More importantly, due to their structural and morphological similarity, GNS can provide a more intimate surface to surface contact with FL-MoS₂ nanosheets to form heterolayered composite compared to other 0D nanoparticles or 1D

nanorods [9,10]. Indeed, the novel heterostructures made by the stacking of GNS and other 2D layered materials together have been paid more and more attention due to their unusual properties and more possibility of application including electronic/photoelectronic devices, clean energy storage and conversion [37]. To date, despite the fact that a few strategies have been developed to prepare SL or FL-MoS₂/graphene composites and great improvement has been achieved on their electrochemical performances, it is still imperative to hunt for a facile and scalable fabricating approach to FL-MoS₂/GNS heterostructural composites.

Recently, we have developed a facile and effective route to prepare SL- or FL-MoS₂/GNS composites by using cationic surfactants [38–40]. Cationic surfactants can be easily adsorbed on the negatively charged GOS surface through electrostatic interaction, and mediate the charge incompatibility between GOS and MoS₂²⁻ (or MoO₄⁴⁻). It is also found that the cationic surfactants showed some ability to control the microstructure (layer number) of MoS₂ in the composites. In our previous works [38,39], the SL- or FL-MoS₂/GNS composites were prepared based on the simultaneous reduction of (NH₄)₂MoS₄ and GOS by hydrazine under refluxing with assistance of different cationic surfactants (CTAB, DTAB, OTAB and TBAB). Hydrothermal route is a facile and effective route for preparing various nanomaterials and nanocomposites, and has shown some advantages in homogeneous nucleation and grain growth of MoS₂ nanosheets compared with the liquid reduction under refluxing. In addition, (NH₄)₂MoS₄ is a special chemical, the price of which is much high than that of the general molybdate (Na₂MoO₄). Thus, FL-MoS₂/GNS composites were also prepared based on hydrothermal reduction of Na₂MoO₄ and L-cysteine in the presence of GOS with assistance of CTAB [40]. It was found that the microstructures and electrochemical performances of the MoS₂/GNS composites prepared by the above two strategies were different; and the FL-MoS₂/GNS composites prepared by hydrothermal method with assistant of 0.01–0.02 M CTAB exhibited better electrochemical lithium storage performance than other samples [39,40]. In order to further study the influence of different cationic surfactants on hydrothermal-synthesized MoS₂/GNS composites and continuously improve their electrochemical performances for LIB application, in this extended work, we demonstrate a facile approach to fabricating FL-MoS₂/GNS composites by a hydrothermal method and post-annealing with the assistance of other three cationic surfactants (DTAB, OTAB and TBAB), which possess different chain lengths and stereo configurations compared to CTAB. The FL-MoS₂/GNS composites were characterized by XRD, SEM, TEM, HRTEM, EDX and Raman spectra. The effects of the different cationic surfactants on the microstructures of the FL-MoS₂/GNS composites and their electrochemical performances of reversible lithium storage were investigated. Electrochemical measurements confirmed that the electrochemical performance of FL-MoS₂/GNS composites for lithium storage was greatly improved compared to the MoS₂. Especially, FL-MoS₂/GNS with ~6 MoS₂ layers prepared with the assistance of 0.02 M OTAB exhibits very high reversible capacity of ~1200 mAh g⁻¹ with excellent cycle stability and enhanced rate capability, which is better than other samples both in this work and in our previous works [38–40].

2. Experimental section

2.1. Synthesis of FL-MoS₂/GNS composites

Graphene oxide was prepared by the oxidization of natural graphite powder using a modified Hummers method [41]. The graphene oxide prepared as such was re-dispersed in deionized water and then exfoliated to graphene oxide sheets (GOS) by

ultrasonication. A brown homogeneous dispersion was obtained by the repeated centrifuging and washing.

In a typical synthesis, 20 mL of 70 mM cationic surfactant (DTAB, OTAB or TBAB) solution was first dropped into 30 mL of GOS (prepared from 3.0 mmol graphite) aqueous dispersion under vigorous stirring. The mixture was stirred at room temperature for 12 h to allow cations (such as OTA^+ , DTA^+ or TBA^+) well adsorbed on the GOS surface by electrostatic interaction. After that, 20 mL solution of 1.5 mmol $\text{Na}_2\text{MoO}_4 \cdot 2\text{H}_2\text{O}$ and 7.5 mmol L-cysteine (L-cys) was dropped into the above mixture with stirring for 30 min. The resultant mixture was transferred into the 100 mL Teflon-lined stainless steel autoclave. The tightly sealed autoclave was maintained at 240 °C for 24 h. After cooling naturally, the black solid product was collected by centrifugation and washed several times with deionized water and ethanol, and dried in the vacuum oven at 80 °C for 12 h. The hydrothermal product was then annealed in the tube furnace at 800 °C for 2 h which was suffused with 10% hydrogen in nitrogen stream flowing at 200 sccm (standard cubic centimeter per minute) to finally form the FL-MoS₂/GNS composites. Three composites, denoted as FL-MoS₂/GNS-D, FL-MoS₂/GNS-O and FL-MoS₂/GNS-T, were respectively synthesized with the assistance of DTAB, OTAB and TBAB. Additionally, the bare MoS₂ was also prepared by a similar synthetic route for comparison.

2.2. Material characterizations

XRD patterns were recorded with a Thermo X'TRA X-ray diffractometer with Cu K α radiation ($\lambda = 0.154056$ nm). Scans were carried out from 5 to 80°. The morphologies of samples were observed by using a SIRION-100 field emission SEM (FESEM). The elemental compositions were analyzed by energy dispersive X-ray spectroscopy (EDX, GENESIS-4000). TEM and HTREM characterizations were performed on a JEOL JEM-2010 TEM operating at 200 kV. Thermogravimetric analysis (TGA) was carried out with a NETZSCH STA 409 PC apparatus at a heating rate of 10 °C min⁻¹ in flowing air. Raman spectra were recorded with 514 nm Ar ion laser at 6 mW for 50 s employing a Jobin Yvon LabRam HR spectrometer.

2.3. Electrochemical measurements

Electrochemical experiments were carried out with 2025 coin-type cells. Lithium foil served as counter electrode and reference electrode, the polypropylene film (Celgard-2300) served as separator, and 1.0 M LiPF₆ solution in EC/DMC (1:1 in volume) as electrolyte. The working electrode was fabricated by casting a slurry of 80 wt% active material, 10 wt% acetylene black and 10 wt% polyvinylidene fluoride in *N*-methyl-2-pyrrolidinone on a copper foil (15 mm in diameter, active material loading of 1.2–1.3 mg). The coated electrode was dried at 120 °C in vacuum for 12 h and then pressed. The test cells were assembled in an argon-filled glove box. Galvanostatic charge/discharge cycles were carried out on a LAND 2001A Battery Tester between 0.005 and 3.00 V. Cyclic voltammetry measurements were carried out on an electrochemical workstation (CHI 660B) in the potential range of 0.01–3.00 V vs. Li/Li⁺ at a scan rate of 0.5 mV s⁻¹. Electrochemical impedance spectroscopy (EIS) was obtained by applying a sine wave with amplitude of 0.5 mV in the frequency range 200 kHz to 0.01 Hz on a PARSTAR 2273.

3. Results and discussions

3.1. Microstructures and morphology

The crystallographic structures of the samples were inspected by XRD. Fig. 1 displays the XRD patterns of the bare MoS₂ and FL-

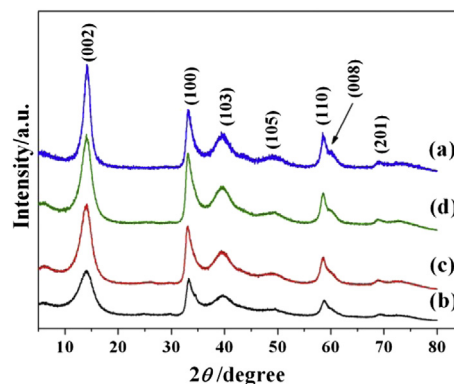


Fig. 1. XRD patterns of the (a) bare MoS₂; (b) FL-MoS₂/GNS-D; (c) FL-MoS₂/GNS-O and (d) FL-MoS₂/GNS-T composites after annealing.

MoS₂/GNS composites after annealing. Despite the broadening of the peaks arising from the nanostructured phases, the diffraction peaks of all samples can be readily ascribed to the hexagonal MoS₂ phase (JCPDS card No. 37-1492). The diffraction peak at $2\theta = 26.6^\circ$ corresponding to the (002) plane of graphene sheets (GNS) is absent in the XRD patterns of the composites, which suggests that the stacking between adjacent graphene sheets is suppressed due to the selective growth of MoS₂ [34]. In addition, all the samples clearly display (002) reflection of MoS₂ at $2\theta = 14.2^\circ$, indicating the *d* spacing of 0.62 nm as calculated by Bragg's equation, which is in agreement with that (0.62 nm) of 2H-MoS₂. Noticeably, the (002) peak of the FL-MoS₂/GNS composites become broadening and lower compared with that of the bare MoS₂, indicating that the (002) plane growth of MoS₂ crystals in the composites was inhibited, resulting in a FL-MoS₂. According to FWHM of (002) reflection using Scherrer's equation, the layer number of MoS₂ sheets could be estimated to be approximately ~12, ~8, ~6 and ~4 layers for the bare MoS₂, FL-MoS₂/GNS-T, FL-MoS₂/GNS-O and FL-MoS₂/GNS-D composites, respectively.

Fig. 2 presents SEM micrographs of the bare MoS₂ and FL-MoS₂/GNS composites after annealing. As shown in Fig. 2a, the MoS₂ exhibits particle-like morphology and the inset clearly reveals that the surface of the particles appears rather coarse because it is covered with curled sheet-like subunits. By contrast, it can be observed from Fig. 2b–d that the FL-MoS₂/GNS composites exhibit a quasi-3D architectural morphology with interconnected porous structures similar to that of self-assembled graphene hydrogels [42,43]. It can also be discerned that the obtained architectures are built up with highly wrinkled 2D nanosheets. No individual MoS₂ particle could be observed from the SEM images, indicating that the MoS₂ are well anchored on the flexible graphene nanosheets. It has been demonstrated that graphene oxide sheets could provide an attractive substrate for the selective nucleation and subsequent growth of MoS₂ [44]. As a consequence, the MoS₂ sheets could be well supported on the surface of GNS to form hetero-layered composites. It is envisioned that the quasi-3D architectural composites could provide the multi-dimensional electron transport pathway, more and shorter channels for the electrolyte access, lithium ion diffusion and insertion/extraction.

TEM and HRTEM characterization was adopted to observe the microstructure of the bare MoS₂ and FL-MoS₂/GNS composites as shown in Fig. 3. The TEM image of the bare MoS₂ (Fig. 3a) ascertains that the basic unit of the particles is bended nanosheets for minimizing the surface energy, consistent with SEM observations. The HRTEM image as shown in Fig. 3b, clearly depicts the well-stacked layered structures of the MoS₂ nanosheets, consisting of about 12 stacked layers. A lattice spacing of 0.62 nm between two adjacent

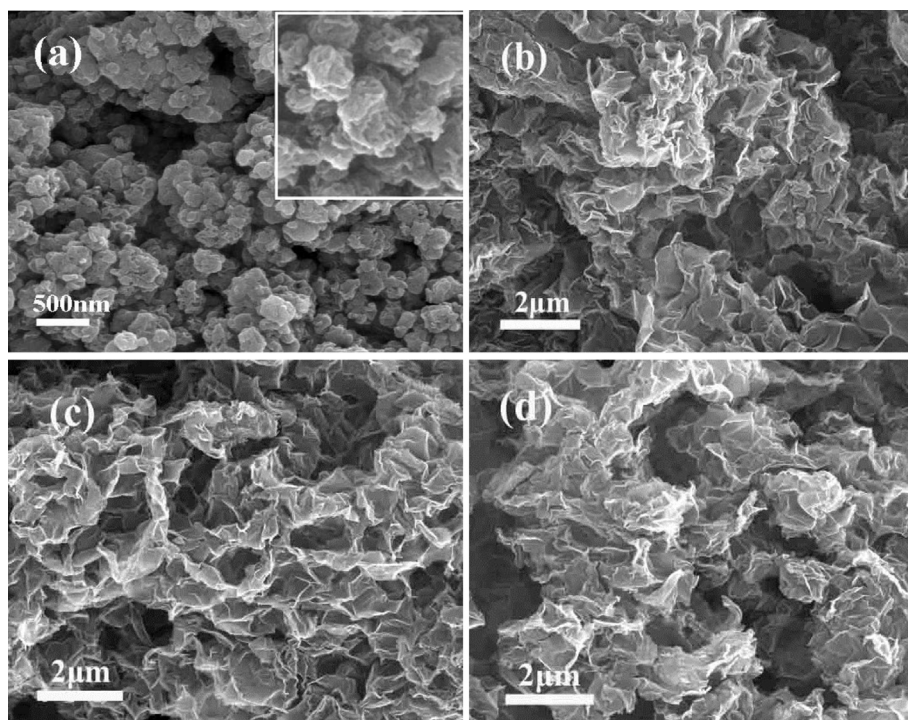


Fig. 2. FESEM images of the (a) bare MoS₂; (b) FL-MoS₂/GNS-D; (c) FL-MoS₂/GNS-O and (d) FL-MoS₂/GNS-T composites after annealing.

lattice planes can be resolved, consistent with the XRD analysis. As for the FL-MoS₂/GNS composites, Fig. 3c–h demonstrates the homogeneous distribution of FL-MoS₂ sheets in the composites. The layer number of FL-MoS₂ is ~ 4 , ~ 6 and ~ 8 layers for the FL-MoS₂/GNS-D, FL-MoS₂/GNS-O and FL-MoS₂/GNS-T composites, respectively. It can be also found that the FL-MoS₂ in the composites possess some defective sites or disordered structures, which could facilitate more lithium ions insertion and improve their electrochemical performances [34,45].

EDX was adopted to identify the elemental compositions of the FL-MoS₂/GNS composites. The results are summarized in Table 1. Table 1 shows that the composites contain C, Mo, S, and a small quantity of O. The calculated atomic ratio of S to Mo element ranges from 1.97 to 2.04, approaching the theoretical stoichiometric value of MoS₂. C element was supplied by both graphene and amorphous carbon stemming from annealing of adsorbed surfactants in hydrothermal products, while a small quantity of O came from the residual oxygen-containing groups of the graphene and amorphous carbon. To further determine the content of MoS₂ in composites, the composites were also characterized by thermogravimetric analysis (TGA). Fig. 4 exhibits a small weight loss below 200 °C due to the vaporization of adsorbed water and a large continuous weight loss in the range of approximately 300–500 °C which was caused by the oxidation of MoS₂, graphene and amorphous carbon. Based on the fact that the final residue is MoO₃ after complete oxidation, the mass fraction of MoS₂ in the composites can be ascertained to be around 59.9%, 69.5% and 76.6% for FL-MoS₂/GNS-D, FL-MoS₂/GNS-O and FL-MoS₂/GNS-T, respectively, which are in good agreement with the results of EDX.

Raman spectroscopy, as a powerful technique for the characterization of the graphene and FL-MoS₂ nanosheets, can provide another proof of the presence of FL-MoS₂ and graphene in the composites. The MoS₂ and FL-MoS₂/GNS composites were examined by Raman spectroscopy as showed in Fig. 5. The bare MoS₂ displays the four dominant peaks along with one weak peak ranging from 250 to 500 cm⁻¹, corresponding to the E_{1g}^1 , LA, E_{2g}^1 ,

A_{1g} , and 2LA(M) mode of the hexagonal MoS₂ crystal, respectively [46,47]. The E_{2g}^1 mode peak at 378.9 cm⁻¹ involves the in-layer displacements of Mo and S atoms, whereas the A_{1g} mode peak at 403.4 cm⁻¹ involves the out-of-layer symmetric displacements of S atoms along the *c*-axis [46,47]. One can find from Fig. 5 that there are significant differences between the Raman spectra of the bare MoS₂ and FL-MoS₂/GNS composites. For the both FL-MoS₂/GNS composites, the E_{1g}^1 , LA and 2LA(M) mode peaks of MoS₂ are strongly suppressed, which agrees with that of few-layer MoS₂ sheets coated on carbon nanotubes [32,48]. In addition, the A_{1g} peaks at 402 cm⁻¹ for FL-MoS₂/GNS-O and 401.1 cm⁻¹ for FL-MoS₂/GNS-D were discerned, in accordance with the few-layer MoS₂ sheets prepared by different methods [24,49]. It has been reported that the SL- or FL-MoS₂ crystal has a down-shift of A_{1g} peak with the decreasing layer number [50]. The frequency shift of the A_{1g} peaks relative to MoS₂ further confirms the few-layer feature of MoS₂ in the FL-MoS₂/GNS composites, consistent with the preceding XRD and HRTEM analysis. To further confirm the existence of graphene in FL-MoS₂/GNS composites, the Raman spectra were collected in the range of 1000–2000 cm⁻¹. As shown in Fig. 5 (right), the D-band and G-band peaks of graphene are observed at ~ 1348 cm⁻¹ and ~ 1580 cm⁻¹ for both FL-MoS₂/GNS composites, which are in good agreement with the hydrazine-reduced graphene and hydrothermal-reduced graphene [51,52]. The G-band represents the vibration of ordered sp²-carbon atoms in a 2D hexagonal lattice, while the D-band is ascribed to edges, defects and disordered carbon. The appearance of G-band and D-band is clearly indicative of the existence of graphene sheets in the composites. Commonly, the relative intensity ratio of I_D/I_G can serve as a convenient measurement of defects in carbon materials. The calculated values of I_D/I_G are 1.41 and 1.34 for FL-MoS₂/GNS-O and FL-MoS₂/GNS-D composites, respectively, which are slightly higher than that of ι -cys reduced graphene (1.08–1.17) [53]. The fact may be caused by the additional amorphous carbon produced from the surfactant carbonization during heat treatment. Therefore, Raman spectroscopy analysis demonstrates the concurrent

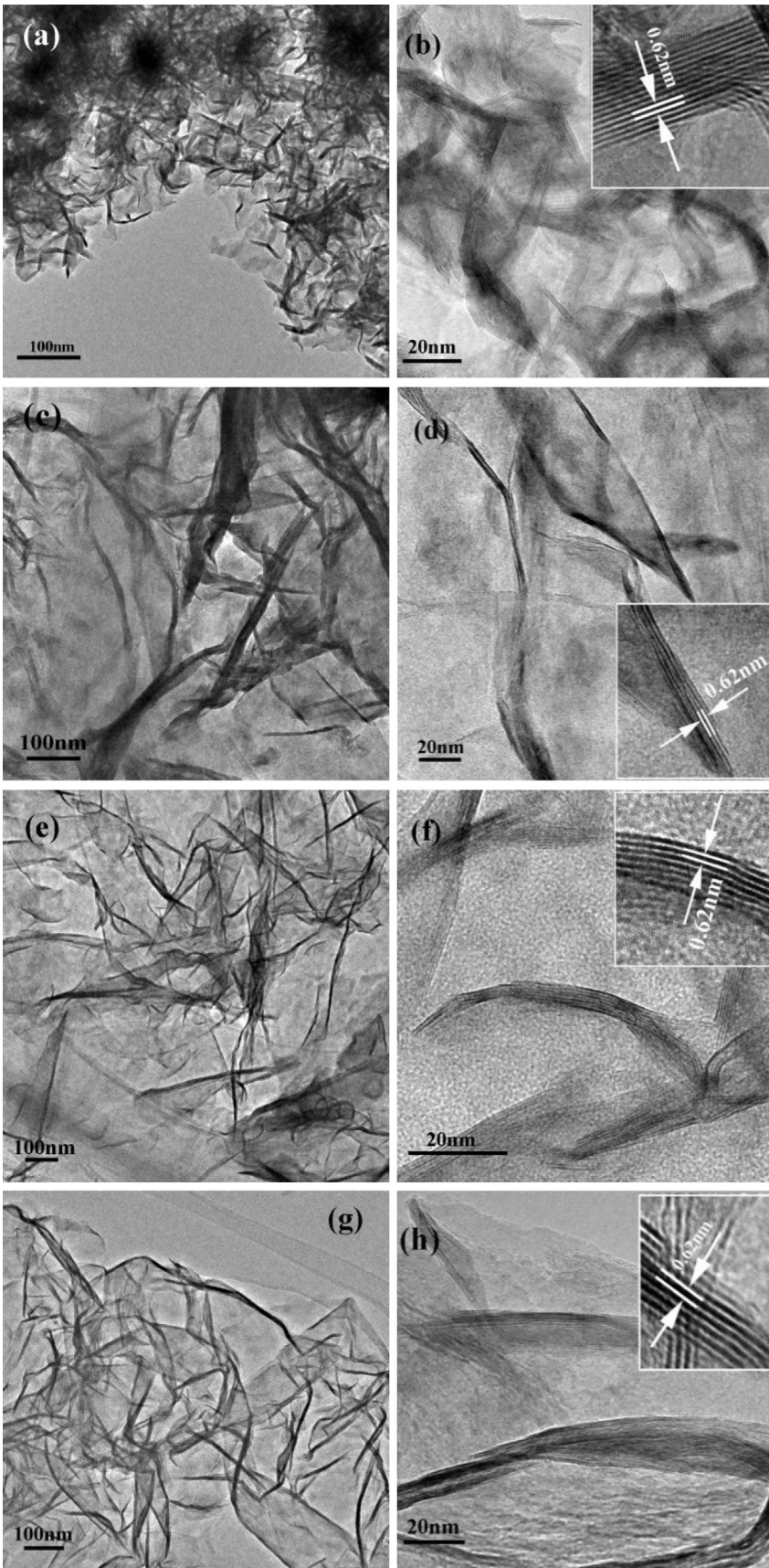


Fig. 3. TEM and HRTEM images of the (a) bare MoS₂; (b) FL-MoS₂/GNS-D; (c) FL-MoS₂/GNS-O and (d) FL-MoS₂/GNS-T composites after annealing.

Table 1

Elemental composition of the FL-MoS₂/GNS composites. S: Mo represents the atomic ratio.

Composition	C/wt%	O/wt%	Mo/wt%	S/wt%	MoS ₂ /wt%	S: Mo
FL-MoS ₂ /GNS-D	34.65	6.63	39.05	19.67	58.72	1.97
FL-MoS ₂ /GNS-O	26.11	6.71	44.14	23.04	70.92	2.04
FL-MoS ₂ /GNS-T	17.01	5.84	51.49	25.65	77.14	1.97

presence of the FL-MoS₂ and graphene nanosheets in the composites.

Based on the above characterization results, the formation process of FL-MoS₂/GNS composites can be illustrated by Scheme 1. GOS is of negatively charged nature due to the presence of abundant oxygen-containing groups on their basal planes and edges [10], which would thwart the approach of anions such as MoO₄^{2−}. The cationic surfactants such as DTAB, OTAB or TBAB, could be easily adsorbed on the highly negatively charged surface of GOS through electrostatic interaction, which can avert the native charge incompatibility between GOS and MoO₄^{2−}. As Na₂MoO₄ aqueous solution is introduced to the suspension of cationic surfactant-adsorbed GOS (QA⁺-GOS, QA⁺ = quaternary ammonium cation), MoO₄^{2−} could be similarly adsorbed on the QA⁺-GOS to form MoO₄^{2−}-QA⁺-GOS complex. During the hydrothermal treatment, MoO₄^{2−} and GOS were reduced to MoS₂ and GNS, respectively. Moreover, MoS₂ layers could selectively grow on the surface of GNS or GOS due to the chemical and electronic coupling between both components [44]. In addition, it was reported that the surface modification of GOS by functional polymers or surfactants may promote their assembly with inorganic species to fabricate composites with hierarchical superstructures by taking advantage of the improved compatibility between these components [54]. Thereafter, the resultant FL-MoS₂/GNS nanosheets could undergo a self-assembly process to form the quasi 3D FL-MoS₂/GNS heterostructural composites in which the π - π stacking and electrostatic attraction between GNS could provide strong cross-linking effect [42,43]. In the ensuing heat treatment, the adsorbed surfactants were carbonized into amorphous carbon. The well-stacking of MoS₂ layers in *c*-direction was restrained by both amorphous carbon and GNS, leading to the formation of FL-MoS₂ nanosheets. Moreover, the preceding XRD and HRTEM characterizations confirmed that the cationic surfactants with different alkyl chain lengths and stereo configurations showed some ability to control the layer numbers of FL-MoS₂ nanosheets in composites. The layer number of MoS₂ in FL-MoS₂/GNS-D composite (~4 layers) is less

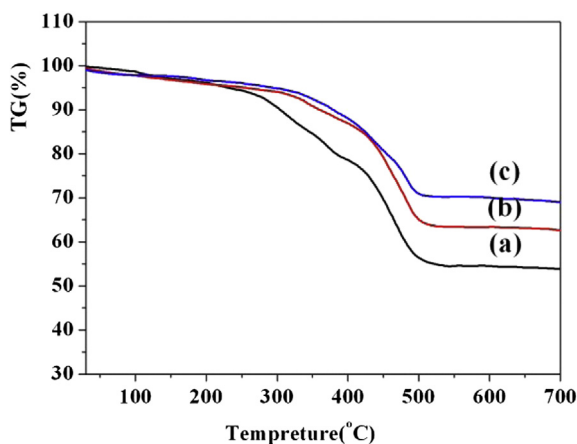


Fig. 4. TGA curves of the (a) FL-MoS₂/GNS-D; (b) FL-MoS₂/GNS-O and (c) FL-MoS₂/GNS-T composites after annealing.

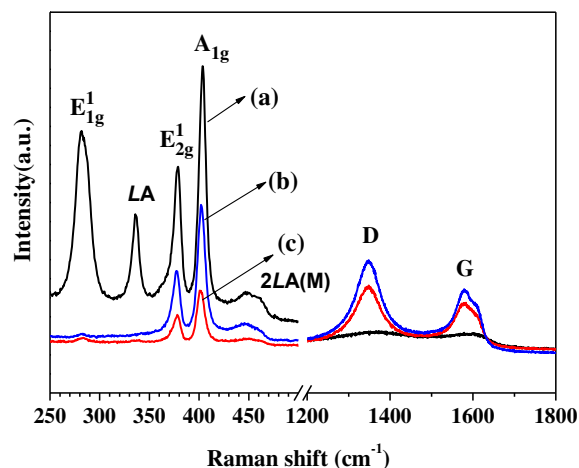
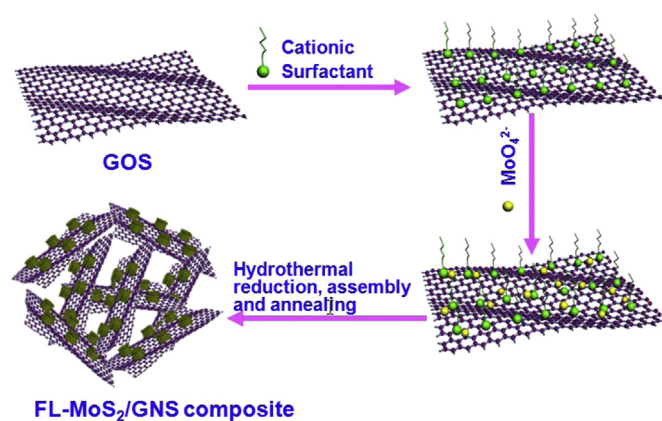


Fig. 5. Raman spectra of the (a) bare MoS₂; (b) FL-MoS₂/GNS-O and (c) FL-MoS₂/GNS-D composites after annealing.

than that of FL-MoS₂/GNS-O (~6 layers) due to the longer straight-line alkyl chain of DTAB than that of OTAB. As for FL-MoS₂/GNS-T composite, TBAB has four butyls linked to N⁺ with sp³-hybrid stereo configuration, which would weaken the interaction between TBA⁺ and GOS due to the hindrance effect, resulting in that the layer number (~8 layer) of MoS₂ in FL-MoS₂/GNS-T is larger compared to other two composites. It was reported that the FL-MoS₂ with 3–5 layer can exhibit very high catalytic active for desulfurization reactions [55]. Therefore, it is reasonably anticipated that FL-MoS₂/GNS composites with FL-MoS₂ (about 4–6 layers) fabricated in this work by a cationic surfactant-assisted hydrothermal route can be applied to both high-performance host electrode materials for electrochemical lithium storage and high-active catalysts for desulfurization reactions.

3.2. Electrochemical performance of lithium storage

The cyclic voltammetry (CV) were conducted to investigate the electrochemical lithium storage of the FL-MoS₂/GNS composite. As shown in Fig. 6, the CV feature of the FL-MoS₂/GNS-O composite electrode is basically similar to that of the MoS₂ electrode; and is also in general agreement with other MoS₂ and MoS₂-based composite electrodes prepared by different methods reported elsewhere [32–35]. It can be seen from Fig. 6b that during the first



Scheme 1. Schematic diagram of the fabrication process of the quasi-3D FL-MoS₂/GNS composites by a facile hydrothermal and a post-annealing route with the assistance of cationic surfactants.

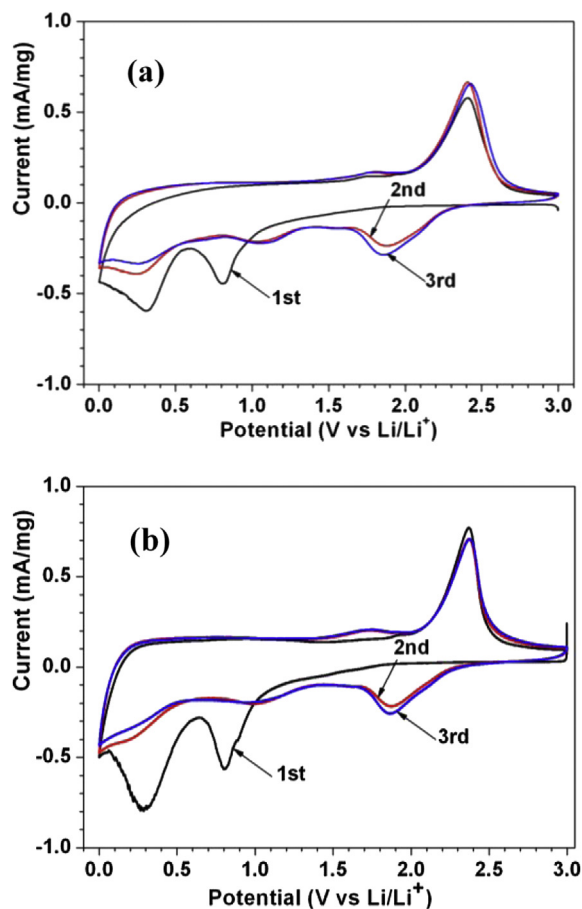


Fig. 6. Cyclic voltammograms of the (a) MoS₂ and (b) FL-MoS₂/GNS-O composite electrodes at a scan rate of 0.5 mV s⁻¹.

cathodic sweep, FL-MoS₂/GNS-O electrode displays two reduction peaks at 0.84 V and 0.35 V, respectively. The first reduction peak at 0.84 V is related to the lithium insertion into the interlayer of MoS₂ to form Li_xMoS₂, accompanied by phase transformation from the 2H (trigonal prismatic) to 1T (octahedral molybdenum coordination) of Li_xMoS₂ [29,30,56]. The second reduction peak at 0.35 V is indicative of the conversion of Li_xMoS₂ into metallic Mo and Li₂S [29,30,34]. In the consecutive cathodic sweeps, three reduction peaks emerging at around 1.84 V, 1.05 V and 0.30 V, respectively, could be ascribed to the following three reactions respectively: $2\text{Li}^+ + \text{S} + 2\text{e}^- \rightarrow \text{Li}_2\text{S}$, $\text{MoS}_2 + x\text{Li}^+ + x\text{e}^- \rightarrow \text{Li}_x\text{MoS}_2$, and $\text{Li}_x\text{MoS}_2 + (4-x)\text{Li}^+ + (4-x)\text{e}^- \rightarrow \text{Mo} + \text{Li}_2\text{S}$ [29,30,34,56]. During the anodic scans, two peaks approximately at 1.81 V and 2.39 V can be observed. The small peak at 1.81 V can be attributed to the partial oxidation of Mo and the dominant peak at 2.39 V may be assigned to the delithiation of Li₂S [30,31,34,56].

Fig. 7 shows the charge/discharge voltage profiles of the MoS₂ and FL-MoS₂/GNS composite electrodes for the initial three cycles, which are in agreement with the above CV study. For instance, Fig. 7c shows that the first discharge voltage profile of the FL-MoS₂/GNS-O electrode can be divided into two plateaus and a sloped region. The plateau at ~1.1 V is indicative of the formation of Li_xMoS₂ [29,30,56], corresponding to the reduction peak at 0.84 V in the CV curves. The plateau at about 0.50 V corresponds to the reduction peak at 0.35 V in the CV curves and can be attributed to conversion reaction process, which first assume the *in situ* decomposition of MoS₂ into Mo particles embedded into a Li₂S matrix and then the formation of a gel-like polymeric layer due to

the electrolyte degradation [29,33,34,56]. The sloped region below 0.50 V could be ascribed to the formation of a solid electrolyte interphase (SEI) layer and lithium storage within the interfaces between two distinct phases of Mo and Li₂S [30,34,35,56]. During the 2nd and 3rd discharge cycles, three potential plateaus can be observed respectively at around 2.0 V, 1.1 V and 0.3 V, which is in agreement with its CV. In the charge process, the potential plateau at 2.2 V can be clearly identified for the first and subsequent cycles, which might be ascribed to the oxidation of Li₂S [30,34,56]. Fig. 7 also shows that the first discharge (lithiation) capacity of MoS₂, FL-MoS₂/GNS-D, FL-MoS₂/GNS-O and FL-MoS₂/GNS-T are 1204, 1449, 1653 and 1363 mAh g⁻¹, respectively, the corresponding reversible (charge) capacities are 882, 1023, 1176 and 935 mAh g⁻¹ with coulombic efficiencies of 73%, 70%, 71%, and 69%. The Coulombic efficiencies of all electrodes are then improved to more than 93% at the 2nd cycle and kept nearly 100% in subsequent cycles. The irreversible capacity loss at the 1st cycle may be mainly attributed to the irreversible processes, such as formation of SEI layer and trapping of some lithium in the lattice or defects [30,34,56]. Compared with MoS₂, the slightly decrease of the 1st Coulombic efficiencies of the FL-MoS₂/GNS composites may be due to the introduction of graphene and amorphous carbon, resulting in more defects in the composites.

In order to discuss the capacity contribution of MoS₂, graphene and amorphous carbon to FL-MoS₂/GNS composites, it needs to determine the contents of three components in the composites. The MoS₂ content could be obtained directly from elemental analysis (Table 1). The determination of the graphene and amorphous carbon contents was indirect (because both components contributed to the C and O signals) and was estimated by the method in our previous studies [34,57]. The calculation results are shown in Table 2. It was reported that the capacity contribution of the exfoliated-MoS₂ nanosheets in MoS₂/PEO composite was up to 1130 mAh g⁻¹ [30] and the specific capacity of the graphene and amorphous carbon was about 800 mAh g⁻¹ and 200 mAh g⁻¹, respectively [57]. Therefore, the specific capacities of FL-MoS₂/GNS composites could be calculated from the composition in Table 2 assuming that these components contributed independently to the composite capacity. It was found that the experimental reversible specific capacities of both FL-MoS₂/GNS-D and FL-MoS₂/GNS-O composites were higher than their calculated values as listed in Table 2. The enhanced specific capacity could attribute to the robust composite structure and synergistic effects between FL-MoS₂ and graphene nanosheets. Whereas the experimental capacity of FL-MoS₂/GNS-T was lower than the calculated value, which might be owing to the fact that the MoS₂ with more layers (~8 layers) in MoS₂/GNS-T delivered low specific capacity, resulting in that its capacity contribution was much less than 1130 mAh g⁻¹.

Fig. 8 exhibits the cycling performance of the MoS₂ and FL-MoS₂/GNS composite electrodes evaluated at a current density of 100 mA g⁻¹ between 0.01 V and 3 V. In the case of MoS₂, Fig. 8a shows a continuous and progressive capacity decay process in which the reversible (charge) capacity gradually decreases with cycle number from an initial capacity of 882 mAh g⁻¹–327 mAh g⁻¹ after 100 cycles, delivering a merely 37% capacity retention. In sharp contrast to that of MoS₂ electrode, the three FL-MoS₂/GNS composite electrodes display significantly improved cycling stability as shown in Fig. 8b–d. After 100 cycles, the reversible capacities of the FL-MoS₂/GNS-D, FL-MoS₂/GNS-O and FL-MoS₂/GNS-T remained as high as 1018 mAh g⁻¹, 1183 mAh g⁻¹ and 901 mAh g⁻¹, with a capacity retention of 99%, 101% and 96% comparing with the original capacities, respectively. Among the three composites, FL-MoS₂/GNS-O demonstrates the highest reversible specific capacity (~1200 mAh g⁻¹), which is also higher

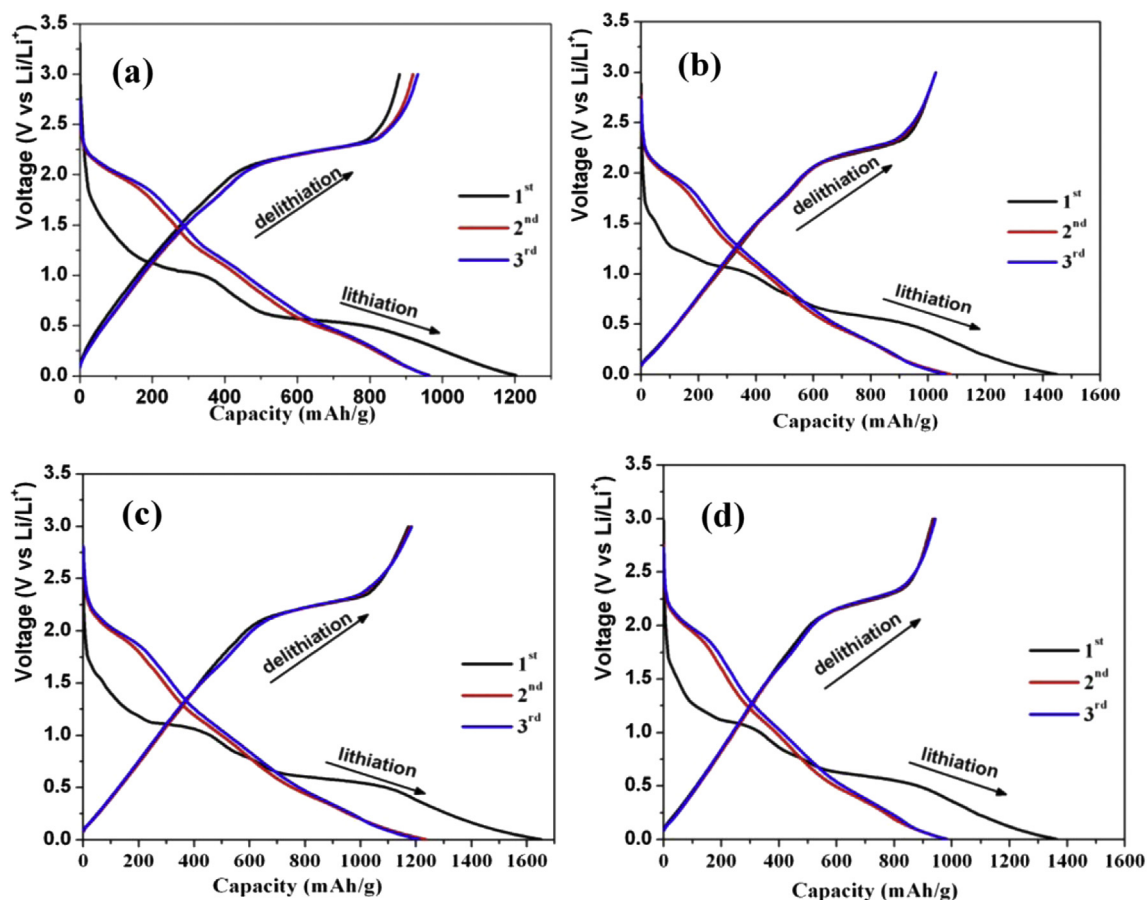


Fig. 7. Charge/discharge voltage profiles of the (a) MoS_2 ; (b) FL- MoS_2 /GNS-D; (c) FL- MoS_2 /GNS-O and (d) FL- MoS_2 /GNS-T composite electrodes at a current density of 100 mA g^{-1} .

than that of the SL- or FL- MoS_2 /GNS composites reported in our previous works [38–40].

To investigate the high rate capability of the MoS_2 and the FL- MoS_2 /GNS composite electrodes, we conducted a multiple-current galvanostatical testing as shown in Fig. 9. The reversible capacities delivered by the MoS_2 at the higher currents of 200, 500, 1000 mA g^{-1} are 684, 482 and 266 mAh g^{-1} , respectively. It is clear that the capacity of the MoS_2 electrode fades rapidly and cannot recover to initial levels even at low discharge currents after high rate cycling. In contrast, the FL- MoS_2 /GNS composites exhibit higher reversible capacities and better rate capabilities than the MoS_2 alone. It is observed from Fig. 9 that the FL- MoS_2 /GNS-D and FL- MoS_2 /GNS-O composite electrodes deliver reversible capacities as high as ~ 769 and 901 mAh g^{-1} with good cycle stability even at a high current density of 1000 mA g^{-1} , respectively. Furthermore, there is no conspicuous capacity decline as the current density drops back to 100 mA g^{-1} after cycling under high current densities. The remarkable electrochemical performances of FL-

MoS_2 /GNS composites can be attributed to the synergistic interactions between FL- MoS_2 and graphene nanosheets and the robust composite structure with quasi-3D architecture. The perfect match of FL- MoS_2 and GNS in the morphology and structure maximize the synergistic interaction [58]. The partial electron transfer from graphene to MoS_2 layers was also demonstrated [58–61], which promote the rapid electron transfer during electrode reaction and improve the electrochemical lithium storage property of the MoS_2 /GNS composite [60,61]. In addition, the unique quasi 3D structure of the composites not only offers an effective buffering matrix to better accommodate the volume

Table 2

The content of MoS_2 , graphene and amorphous carbon in the composites and the calculated specific capacities.

Composites	MoS_2 /wt%	GNS/wt%	Amorphous carbon/wt%	Calculated specific capacity/ mAh g^{-1}	Experimental specific capacity at 1st cycle/ mAh g^{-1}
FL- MoS_2 /GNS-D	58.72	14.31	26.97	832	1023
FL- MoS_2 /GNS-O	70.92	17.28	11.80	1018	1176
FL- MoS_2 /GNS-T	77.14	18.79	4.07	1089	935

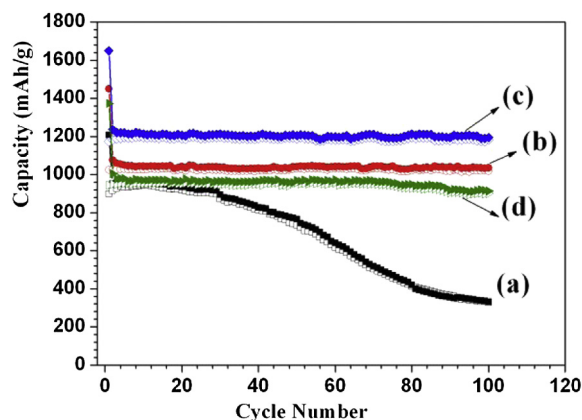


Fig. 8. Cycle performance of the (a) MoS_2 ; (b) FL- MoS_2 /GNS-D; (c) FL- MoS_2 /GNS-O and (d) FL- MoS_2 /GNS-T composite electrodes at a current density of 100 mA g^{-1} .

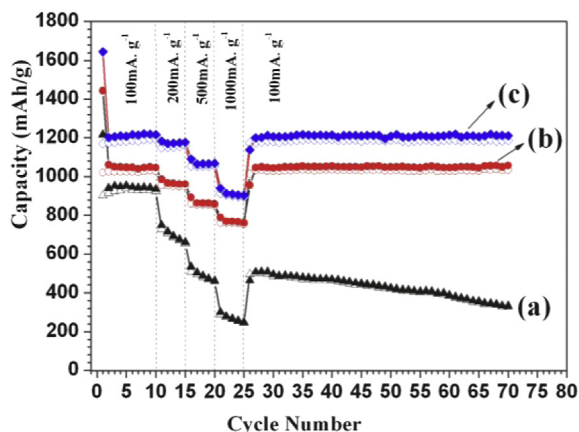


Fig. 9. Rate capabilities of the (a) MoS₂; (b) FL-MoS₂/GNS-D; (c) FL-MoS₂/GNS-O electrodes at different current densities.

change of MoS₂ during cycling, but also provides more and shorter channels for the access of electrolyte and the fast diffusion of lithium ions. Thus, FL-MoS₂/GNS composite electrodes exhibited much higher specific capacity and superior cycle performance compared to the MoS₂ electrode.

EIS were measured to better understand why the FL-MoS₂/GNS composite electrodes exhibit the excellent electrochemical performance. Fig. 10a shows the Nyquist plots of the MoS₂ and FL-MoS₂/GNS composite electrodes at the 8th cycle, and Fig. 10b is the equivalent circuit model for the impedance response. The Nyquist plots consist of two semicircles at the high and medium frequency regions followed by a slope line at the low frequency region. The high frequency semicircle in Fig. 10a could be ascribed to resistance R_f and CPE₁ of the SEI, and medium frequency semicircle to the charge transfer resistance of the electrode reaction R_{ct} and CPE₂ of the electrode–electrolyte interface, and the slope line in the low

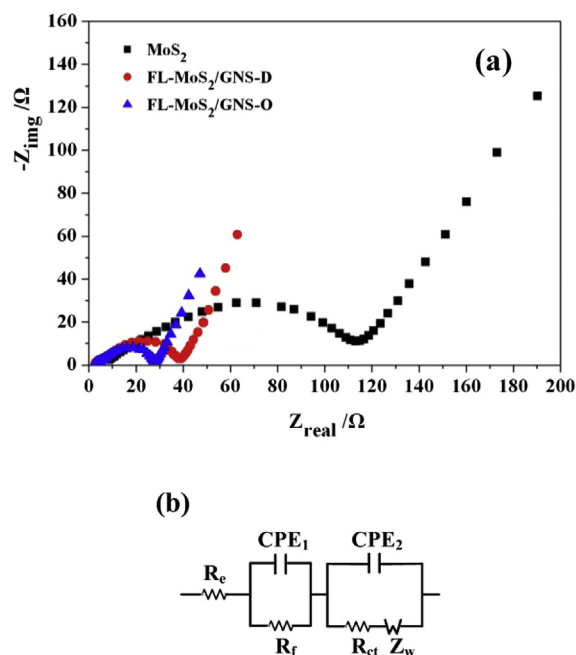


Fig. 10. (a) Nyquist plots of the MoS₂ and FL-MoS₂/GNS composite electrodes obtained by applying a sine wave with amplitude of 5.0 mV over the frequency range from 200 kHz to 0.01 Hz; (b) equivalent circuit model of the studied system. CPE represents the constant phase element, $Z_{CPE} = \{Q(j\omega)^n\}$, $0 < n < 1$.

Table 3

R_f and R_{ct} values of the MoS₂ and FL-MoS₂/GNS composite electrodes.

Electrode	MoS ₂	FL-MoS ₂ /GNS-D	FL-MoS ₂ /GNS-O
R_f/Ω	24.90	4.41	3.59
R_{ct}/Ω	83.92	32.55	22.41

frequency region to Li⁺ diffusion processes impedance Z_w (warburg impedance) [34]. It can be observed that the diameter of the semicircle at high frequencies is remarkably reduced in the plot of FL-MoS₂/GNS composites, compared with that of the MoS₂ alone, indicating the greatly decreased charge-transfer resistance at the electrode/electrolyte interface due to the combination with conductive graphene and amorphous carbon. The R_f and R_{ct} can be obtained by data fitting according to the equivalent circuit model in Fig. 10b and the results are summarized in Table 3. It is clearly demonstrated that the R_f and R_{ct} values of the FL-MoS₂/GNS are much less than those of MoS₂ alone, which confirm the reduction in contact resistance and charge transfer resistance in Li⁺ insertion/extraction reactions. The improvement in electrochemical kinetic parameters is attributed to the synergistic interaction between FL-MoS₂ and graphene nanosheets and the partial electron transfer from graphene to FL-MoS₂ [58–61].

4. Conclusion

In summary, the FL-MoS₂/GNS heterolayered composites were successfully synthesized via a facile hydrothermal reaction plus a subsequent annealing process with assistant of different cationic surfactants (DTAB, OTAB and TBAB). The obtained FL-MoS₂/GNS composites exhibited remarkable electrochemical performances including highly reversible specific capacity, excellent cycling performance and enhanced high-rate capability, among which the FL-MoS₂/GNS-O behaved best. The remarkable electrochemical performances of the FL-MoS₂/GNS composites can be attributed to the synergistic interaction between FL-MoS₂ and GNS, and the robust quasi-3D architectures of the composites, which are favorable for rapid lithium diffusion, electron transfer and electrolyte access during electrochemical lithiation/delithiation. The strategy presented in this work is facile and efficient, and can be scaled up for the large-scale production of the heterolayered composites made from GNS and other 2D nanosheets.

Acknowledgments

This work is financially supported by the International Science and Technology Cooperation Program of China (2012DFG42100), the National Natural Science Foundation of China (21173190), the Doctoral Program of Higher Education of China (2011010113003), the International Science and Technology Cooperation Program of Zhejiang Province (2013C24011), Postdoctoral Science Fund of China (2013M540485) and Open Fund from Zhejiang Institute of Energy and Nuclear Application Technology. Lee JY is also grateful for the financial support from the Agency for Science, Technology and Research under Project No. 1220203049 (R279-000-370-305).

References

- [1] C. de las Casas, W.Z. Li, J. Power Sources 208 (2012) 74–85.
- [2] N.S. Choi, Z.H. Chen, S.A. Freunberger, X.L. Ji, Y.K. Sun, K. Amine, G. Yushin, L.F. Nazar, J. Cho, P.G. Bruce, Angew. Chem. Int. Ed. 51 (2012) 9994–10024.
- [3] J.M. Tarascon, M. Armand, Nature 414 (2001) 359–367.
- [4] K. Zaghib, A. Mauger, H. Groult, J.B. Goodenough, C.M. Julien, Materials 6 (2013) 1028–1049.
- [5] J.H. Liu, X.W. Liu, Adv. Mater. 24 (2012) 4097–4111.
- [6] M. Chhowalla, H.S. Shin, G. Eda, L.J. Li, K.P. Loh, H. Zhang, Nat. Chem. 5 (2013) 263–275.

- [7] X. Huang, Z.Y. Yin, S.X. Wu, X.Y. Qi, Q.Y. He, Q.C. Zhang, Q.Y. Yan, F. Boey, H. Zhang, *Small* 7 (2011) 1876–1902.
- [8] Y.Q. Sun, Q.O. Wu, G.Q. Shi, *Energy Environ. Sci.* 4 (2011) 1113–1132.
- [9] C.H. Xu, B.H. Xu, Y. Gu, Z.G. Xiong, J. Sun, X.S. Zhao, *Energy Environ. Sci.* 6 (2013) 1388–1414.
- [10] S. Han, D.Q. Wu, S. Li, F. Zhang, X.L. Feng, *Small* 9 (2013) 1173–1187.
- [11] X. Huang, Z.Y. Zeng, H. Zhang, *Chem. Soc. Rev.* 42 (2013) 1934–1946.
- [12] J.H. Zhan, Z.D. Zhang, X.F. Qian, C. Wang, Y. Xie, Y.T. Qian, *J. Solid State Chem.* 141 (1998) 270–273.
- [13] H. Li, G. Lu, Z.Y. Yin, Q.Y. He, Q. Zhang, H. Zhang, *Small* 8 (2012) 682–686.
- [14] Z.Y. Yin, H. Li, L. Jiang, Y.M. Shi, Y.H. Sun, G. Lu, Q. Zhang, X.D. Chen, H. Zhang, *ACS Nano* 6 (2012) 74–80.
- [15] H. Li, G. Lu, Y. Wang, Z. Yin, C. Cong, Q. He, L. Wang, F. Ding, T. Yu, H. Zhang, *Small* 9 (2013) 1974–1981.
- [16] J.N. Coleman, M. Lotya, A. O'Neill, S.D. Bergin, P.J. King, U. Khan, K. Young, A. Gaucher, S. De, R.J. Smith, I.V. Shvets, S.K. Arora, G. Stanton, H.-Y. Kim, K. Lee, G.T. Kim, G.S. Duesberg, T. Hallam, J.J. Boland, J.J. Wang, J.F. Donegan, J.C. Grunlan, G. Moriarty, A. Shmeliov, R.J. Nicholls, J.M. Perkins, E.M. Grievson, K. Theuvsen, D.W. McComb, P.D. Nellist, V. Nicolosi, *Science* 331 (2011) 568–571.
- [17] K.G. Zhou, N.N. Mao, H.X. Wang, Y. Peng, H.L. Zhang, *Angew. Chem. Int. Ed.* 50 (2011) 10839–10842.
- [18] A. O'Neill, U. Khan, J.N. Coleman, *Chem. Mater.* 24 (2012) 2414–2421.
- [19] R.J. Smith, P.J. King, M. Lotya, C. Wirtz, U. Khan, S. De, A. O'Neill, G.S. Duesberg, J.C. Grunlan, G. Moriarty, J. Chen, J. Wang, A.I. Minett, V. Nicolosi, J.N. Coleman, *Adv. Mater.* 23 (2011) 3944–3948.
- [20] G. Cunningham, M. Lotya, C.S. Cucinotta, S. Sanvito, S.D. Bergin, R. Menzel, M.S.P. Shaffer, J.N. Coleman, *ACS Nano* 6 (2012) 3468–3480.
- [21] Z. Zeng, T. Sun, J. Zhu, X. Huang, Z. Yin, G. Lu, Z. Fan, Q. Yan, H.H. Hng, H. Zhang, *Angew. Chem. Int. Ed.* 51 (2012) 9052–9056.
- [22] S. Wu, Z. Zeng, Q. He, Z. Wang, S.J. Wang, Y. Du, Z. Yin, X. Sun, W. Chen, H. Zhang, *Small* 8 (2012) 2264–2270.
- [23] A. Castellanos-Gomez, M. Barkelid, A.M. Goossens, V.E. Calado, H.S.J. van der Zant, G.A. Steele, *Nano Lett.* 12 (2012) 3187–3192.
- [24] H.S.S.R. Matte, A. Gomathi, A.K. Manna, D.J. Late, R. Datta, S.K. Pati, C.N.R. Rao, *Angew. Chem. Int. Ed.* 49 (2010) 4059–4062.
- [25] Y.D. Liu, L. Ren, X. Qi, L.W. Yang, G.L. Hao, J. Li, X.L. Wei, J.X. Zhong, *J. Alloys Compd.* 571 (2013) 37–42.
- [26] I. Zafropoulou, M.S. Katsiotis, N. Boukos, M.A. Karakassides, S. Stephen, V. Tzitzios, M. Fardis, R.V. Vlades, S.M. Alhassan, G. Papavassiliou, *J. Phys. Chem. C* 117 (2013) 10135–10142.
- [27] S. Ding, D. Zhang, J.S. Chen, X.W. Lou, *Nanoscale* 4 (2012) 95–98.
- [28] H. Hwang, H. Kim, J. Cho, *Nano Lett.* 11 (2011) 4826–4830.
- [29] G. Du, Z. Guo, S. Wang, R. Zeng, Z. Chen, H. Liu, *Chem. Commun.* 46 (2010) 1106–1108.
- [30] J. Xiao, D. Choi, L. Cosimbescu, P. Koeh, J. Liu, J.P. Lemmon, *Chem. Mater.* 22 (2010) 4522–4524.
- [31] S. Ding, J.S. Chen, X.W. Lou, *Chem. Eur. J.* 17 (2011) 13142–13145.
- [32] K. Bindumadhavan, S.K. Srivastava, S. Mahanty, *Chem. Commun.* 49 (2013) 1823–1825.
- [33] S.K. Park, S.H. Yu, S. Woo, B. Quan, D.C. Lee, M.K. Kim, Y.E. Sung, Y. Piao, *Dalton Trans.* 42 (2013) 2399–2405.
- [34] K. Chang, W.X. Chen, *ACS Nano* 5 (2011) 4720–4728.
- [35] H. Yu, C. Ma, B. Ge, Y. Chen, Z. Xu, C. Zhu, C. Li, Q. Ouyang, P. Gao, J. Li, C. Sun, L. Qi, Y. Wang, F. Li, *Chem. Eur. J.* 19 (2013) 5818–5823.
- [36] X. Zhou, L.J. Wan, Y.G. Guo, *Chem. Commun.* 49 (2013) 1838–1840.
- [37] A.K. Geim, I.V. Grigorieva, *Nature* 499 (2013) 419–425.
- [38] Z. Wang, L. Ma, W.X. Chen, G.C. Huang, D.Y. Chen, L.B. Wang, J.Y. Lee, *RSC Adv.* 3 (2013) 21675–21684.
- [39] Z. Wang, T. Chen, W.X. Chen, K. Chang, L. Ma, G.C. Huang, D.Y. Chen, J.Y. Lee, *J. Mater. Chem. A* 1 (2013) 2202–2210.
- [40] G.C. Huang, T. Chen, W.X. Chen, Z. Wang, K. Chang, L. Ma, F.H. Huang, D.Y. Chen, J.Y. Lee, *Small* 9 (2013) 3693–3703.
- [41] W.S. Hummers, R.E. Offeman, *J. Am. Chem. Soc.* 80 (1958), 1339.
- [42] M.A. Worsley, P.J. Pauzauskie, T.Y. Olson, J. Biener, J.H. Satcher, T.F. Baumann, *J. Am. Chem. Soc.* 132 (2010) 14067–14069.
- [43] Y.X. Xu, K.X. Sheng, C. Li, G.Q. Shi, *ACS Nano* 4 (2010) 4324–4330.
- [44] E.G.S. Firmiano, M.A.L. Cordeiro, A.C. Rabelo, C.J. Dalmaschio, A.N. Pinheiro, E.C. Pereira, E.R. Leite, *Chem. Commun.* 48 (2012) 7687–7689.
- [45] K. Chang, W.X. Chen, L. Ma, H. Li, H. Li, F. Huang, Z. Xu, Q. Zhang, J.Y. Lee, *J. Mater. Chem.* 21 (2011) 6251.
- [46] G. Plechinger, S. Heydrich, J. Eroms, D. Weiss, C. Schuller, T. Korn, *Appl. Phys. Lett.* 101 (2012) 101906–101908.
- [47] H. Li, Q. Zhang, C.C.R. Yap, B.K. Tay, T.H.T. Edwin, A. Olivier, D. Baillargeat, *Adv. Funct. Mater.* 22 (2012) 1385–1390.
- [48] S.Y. Tai, C.J. Liu, S.W. Chou, F.S.S. Chien, J.Y. Lin, T.W. Lin, *J. Mater. Chem.* 22 (2012) 24753–24759.
- [49] K. Zhang, H.J. Kim, X. Shi, J.T. Lee, J.M. Choi, M.S. Song, J.H. Park, *Inorg. Chem.* 52 (2013) 9807–9812.
- [50] B. Chakraborty, H. Matte, A.K. Sood, C.N.R. Rao, *J. Raman Spectrosc.* 44 (2013) 92–96.
- [51] C. Bosch-Navarro, E. Coronado, C. Marti-Gastaldo, J.F. Sanchez-Royo, M. Gomez Gomez, *Nanoscale* 4 (2012) 3977–3982.
- [52] O.A. V. C. A. Caballero, J. Morales, *Nanoscale* 4 (2012) 2083–2092.
- [53] D. Chen, L. Li, L. Guo, *Nanotechnology* 22 (2011) 325601–325608.
- [54] K. Zhang, L. Mao, L.L. Zhang, H.S. On Chan, X.S. Zhao, J. Wu, *J. Mater. Chem.* 21 (2011) 7302–7307.
- [55] J. Kibsgaard, A. Tuxen, K.G. Knudsen, M. Brorson, H. Topsoe, E. Laegsgaard, J.V. Lauritsen, F. Besenbacher, *J. Catal.* 272 (2010) 195–203.
- [56] X. Fang, X. Yu, S. Liao, Y. Shi, Y.S. Hu, Z. Wang, G.D. Stucky, L. Chen, *Micro-porous Mesoporous Mater.* 151 (2012) 418–423.
- [57] K. Chang, W.X. Chen, *J. Mater. Chem.* 21 (2011) 17175–17184.
- [58] V.O. Koroteev, L.G. Bulusheva, A.V. Okotrub, N.F. Yudanov, D.V. Vyalikh, *Phys. Status Solidi B* 248 (2011) 2740–2743.
- [59] V.O. Koroteev, L.G. Bulusheva, I.P. Asanov, E.V. Shlyakhova, D.V. Vyalikh, A.V. Okotrub, *J. Phys. Chem. C* 115 (2011) 21199–21204.
- [60] X.B. Chen, J.H. He, D. Srivastava, J. Li, *Appl. Phys. Lett.* 100 (2012) 263901.
- [61] X.D. Li, S. Yu, S.Q. Wu, Y.H. Wen, S. Zhou, Z.Z. Zhu, *J. Phys. Chem. C* 117 (2013) 15347–15353.